

See discussions, stats, and author profiles for this publication at: <https://www.researchgate.net/publication/259240522>

# Morphology-Dependent Properties of $\text{MnO}_x/\text{ZrO}_2-\text{CeO}_2$ Nanostructures for the Selective Catalytic Reduction of NO with $\text{NH}_3$

ARTICLE in THE JOURNAL OF PHYSICAL CHEMISTRY C · MAY 2013

Impact Factor: 4.77 · DOI: 10.1021/jp400984z

CITATIONS

35

READS

88

## 8 AUTHORS, INCLUDING:



Ruihua Gao

Fudan University

28 PUBLICATIONS 812 CITATIONS

SEE PROFILE



Phornphimon Maitarad

Shanghai University

17 PUBLICATIONS 310 CITATIONS

SEE PROFILE



Thanyada Rungrotmongkol

Chulalongkorn University

61 PUBLICATIONS 703 CITATIONS

SEE PROFILE



Jianping Zhang

Independent Researcher

100 PUBLICATIONS 2,037 CITATIONS

SEE PROFILE

# Morphology-Dependent Properties of $\text{MnO}_x/\text{ZrO}_2\text{--CeO}_2$ Nanostructures for the Selective Catalytic Reduction of NO with $\text{NH}_3$

Ruihua Gao,<sup>†,§</sup> Dengsong Zhang,<sup>\*,†</sup> Phornphimon Maitarad,<sup>†</sup> Liyi Shi,<sup>\*,‡</sup> Thanyada Rungrotmongkol,<sup>||</sup> Hongrui Li,<sup>†</sup> Jianping Zhang,<sup>†,‡</sup> and Weiguo Cao<sup>‡</sup>

<sup>†</sup>Research Center of Nano Science and Technology, Shanghai University, Shanghai 200444, China

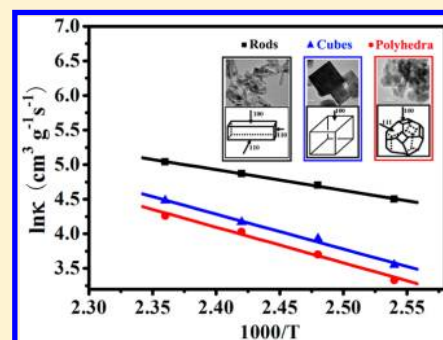
<sup>‡</sup>Department of Chemistry, Shanghai University, Shanghai, 200444, China

<sup>§</sup>State Key Laboratory of Molecular Engineering of Polymers, Department of Macromolecular Science, Fudan University, Shanghai, 200433, China

<sup>||</sup>Department of Biochemistry, Faculty of Science, Chulalongkorn University, 254 Phayathai Road, Bangkok 10330, Thailand

## S Supporting Information

**ABSTRACT:** The morphology effect of  $\text{ZrO}_2\text{--CeO}_2$  on the performance of  $\text{MnO}_x/\text{ZrO}_2\text{--CeO}_2$  catalyst for the selective catalytic reduction of NO with ammonia was investigated. The catalytic tests showed that the  $\text{MnO}_x/\text{ZrO}_2\text{--CeO}_2$  nanorods achieved significantly higher NO conversions than the nanocubes and nanopolyhedra. The catalytic tests also showed that the  $\text{MnO}_x/\text{ZrO}_2\text{--CeO}_2$  nanorods achieved a significantly higher rate constant with respect to NO conversion than that of the nanocubes and nanopolyhedra. On the nanorods, the apparent activation energy is  $25 \text{ kJ mol}^{-1}$ , which was much lower than the values of nanocubes and nanopolyhedra ( $42$  and  $43 \text{ kJ mol}^{-1}$ ). The high resolution transmission electron microscopy showed that the nanorods predominately exposed  $\{110\}$  and  $\{100\}$  planes. It was demonstrated that the  $\text{ZrO}_2\text{--CeO}_2$  nanorods had a strong interaction with  $\text{MnO}_x$  species, which resulted in great superiority for the selective catalytic reduction of NO. The excellent catalytic activity of the  $\text{MnO}_x/\text{ZrO}_2\text{--CeO}_2$  nanorods should be attributed to the  $\text{Mn}^{4+}$  species, adsorbed surface oxygen and oxygen vacancies which are associated with their exposed  $\{110\}$  and  $\{100\}$  planes.



## 1. INTRODUCTION

Nitrogen oxides ( $\text{NO}_x$ ) emitted from stationary sources and automobiles are major causes for acid rain, smog, and ozone depletion. The selective catalytic reduction (SCR) of  $\text{NO}_x$  to  $\text{N}_2$  using  $\text{NH}_3$  as a reductant is now considered to be the most effective process for the treatment of nitrogen oxides from stationary sources.<sup>1–3</sup>  $\text{V}_2\text{O}_5\text{--WO}_3$  ( $\text{MoO}_3$ )/ $\text{TiO}_2$  has been widely used as an industrial catalyst. This kind of catalyst shows high  $\text{NO}_x$  reduction efficiencies and a high resistance to  $\text{SO}_2$  poisoning. However, the reaction should be operated at relatively high temperatures and the SCR reactor is located upstream before the dust removal or desulfurizer device to avoid reheating of the flue gas. Therefore, the catalysts are more poisoned by the high concentration of dust and  $\text{SO}_2$ . Thus, the design of the highly active catalysts for low-temperature SCR located downstream after the dust removal or desulfurizer device becomes important.

Among many transition metal oxides, manganese oxide-containing catalysts exhibited a relatively high conversion of  $\text{NO}_x$  in the  $\text{NH}_3\text{--SCR}$ .<sup>4–7</sup> Especially, the  $\text{CeO}_2$  promoted  $\text{MnO}_x$  catalysts have been studied extensively as low temperature SCR catalysts.<sup>8–13</sup> In recent years, many low dimensional  $\text{CeO}_2$  nanomaterials, such as ceria nanorods, nanocubes, nanopolyhedra, and so on, have been reported by us and other research groups.<sup>14–16</sup> Generally, different  $\text{CeO}_2$  shapes

expose different lattice planes in crystal structures. For example,  $\text{CeO}_2$  nanorods preferentially expose four  $\{110\}$  and two  $\{100\}$  planes, while  $\text{CeO}_2$  nanopolyhedra expose eight  $\{111\}$  or eight  $\{111\}$  and six  $\{100\}$  planes.<sup>16,17</sup> According to density functional theory,<sup>17,18</sup> the formation energy of an oxygen vacancy on the different planes follows the sequence  $\{110\} < \{100\} < \{111\}$ , while the chemical activity of these planes follows the opposite sequence. Up until now, there are several papers that have shown the results about the shape effects of  $\text{CeO}_2$  in NO reduction by CO,<sup>19</sup> water-gas shift reaction,<sup>20</sup> and CO oxidation.<sup>21,22</sup> Liu et al.<sup>19</sup> investigated the catalytic performance of different CuO-supported ceria nanoshapes for NO reduction by CO. They found that there was a strong synergistic interaction between CuO and the exposed  $\{110\}$  planes of the  $\text{CeO}_2$  nanorods, which led to a high activity for NO reduction to  $\text{N}_2$ , while the weak interaction between CuO and the  $\{100\}$  plane of  $\text{CeO}_2$  cubes determined its lower activity at low temperatures. Mai et al.<sup>16</sup> reported that  $\text{CeO}_2$  nanorods and nanocubes were more active for CO oxidation than the  $\{111\}$ -plane-dominated  $\text{CeO}_2$  nanoparticles due to the presence of more  $\{110\}/\{100\}$  crystal planes. They also found that the

Received: January 29, 2013

Revised: April 5, 2013

Published: April 26, 2013

oxygen storage took place at the surface as well as the bulk over nanorods and nanocubes, whereas the oxygen storage was limited to the bulk in nanoparticles. Recently, our group found that the Ni/CeO<sub>2</sub> nanorod catalysts displayed a more excellent catalytic activity and higher coke resistance as compared with Ni/CeO<sub>2</sub> nanopolyhedra for the CO<sub>2</sub> reforming of methane.<sup>23</sup> We found that the oxygen vacancies and the mobility of lattice oxygen had been dependent on the morphology of the CeO<sub>2</sub> support, which resulted in the different activity performance.

So far, the morphology dependence of ceria nanomaterials in manganese oxides for NH<sub>3</sub>-SCR of NO has not been reported yet. The pure CeO<sub>2</sub> is not suitable for the practical application because of the low thermal stability and the loss of surface area at high temperatures.<sup>9</sup> Some researchers found that the thermal stability of CeO<sub>2</sub> is significantly improved by adding zirconium oxide.<sup>24,25</sup>

In this work, we design the synthesis of MnO<sub>x</sub>/ZrO<sub>2</sub>-CeO<sub>2</sub> nanomaterials and investigate the effect of the morphology of ZrO<sub>2</sub>-CeO<sub>2</sub> on the activity of MnO<sub>x</sub>/ZrO<sub>2</sub>-CeO<sub>2</sub> for the SCR of NO with NH<sub>3</sub>. Three different shapes of ZrO<sub>2</sub>-CeO<sub>2</sub> nanomaterials, such as nanorods, nanocubes, and nanopolyhedra, were prepared by a hydrothermal method. A wet impregnation method was used to incorporate manganese oxides over the ZrO<sub>2</sub>-CeO<sub>2</sub> nanomaterials. The catalytic performance of the MnO<sub>x</sub>/ZrO<sub>2</sub>-CeO<sub>2</sub> nanomaterials with various shapes was examined in the NH<sub>3</sub>-SCR of NO.

## 2. EXPERIMENT

**2.1. Catalyst Preparation.** The chemicals were purchased from Sinopharm Chemical Reagent Company. All of these chemicals were used without further purification.

ZrO<sub>2</sub>-CeO<sub>2</sub> nanorods, ZrO<sub>2</sub>-CeO<sub>2</sub> nanocubes, and ZrO<sub>2</sub>-CeO<sub>2</sub> nanopolyhedra were prepared by a hydrothermal method varying the amount of reactant and hydrothermal temperatures.<sup>16</sup> The molar ratios of Zr/Zr+Ce over the ZrO<sub>2</sub>-CeO<sub>2</sub> were all 10%. Typically, 4.5 mmol of Ce(NO<sub>3</sub>)<sub>3</sub>·6H<sub>2</sub>O, 0.5 of mmol Zr(NO<sub>3</sub>)<sub>4</sub>·5H<sub>2</sub>O, and an appropriate amount of NaOH (19.2 g for nanorods and nanocubes, 0.32 g for nanopolyhedra) were dissolved into 40 mL of distilled water, respectively. Then, the solution was mixed together and kept stirring for 30 min. The mixture was then transferred to a stainless steel reaction tank with polytetrafluoroethylene (PTFE) lining (100 mL) and maintained at an appropriate temperature (100 °C for nanorods, 180 °C for nanocubes and nanopolyhedra) for 24 h. After centrifugation and washing with water and ethanol, the precipitate was dried at 80 °C overnight, and finally calcined at 400 °C for 5 h in air. The prepared ZrO<sub>2</sub>-CeO<sub>2</sub> nanorods, ZrO<sub>2</sub>-CeO<sub>2</sub> nanocubes, and ZrO<sub>2</sub>-CeO<sub>2</sub> nanopolyhedra were, respectively, denoted as ZrCe-NR, ZrCe-NC, and ZrCe-NP. The MnO<sub>x</sub>/ZrO<sub>2</sub>-CeO<sub>2</sub> catalysts were prepared by a wet incipient impregnation method. The prepared ZrCe-NR, ZrCe-NC, and ZrCe-NP were used as support materials. The manganese nitrate solution (50%) was used as the source of manganese. The manganese loading was selected as 5 wt %. The MnO<sub>x</sub>/ZrO<sub>2</sub>-CeO<sub>2</sub> nanorods, MnO<sub>x</sub>/ZrO<sub>2</sub>-CeO<sub>2</sub> nanocubes, and MnO<sub>x</sub>/ZrO<sub>2</sub>-CeO<sub>2</sub> nanopolyhedra were denoted as MnZrCe-NR, MnZrCe-NC, and MnZrCe-NP, respectively.

**2.2. Characterization and DFT Calculations.** Nitrogen sorption isotherms of the samples were measured at -196 °C using an ASAP 2010 Micromeritics instrument. The specific surface area of the samples was calculated by the Brunauer-Emmett-Teller (BET) method. Powder X-ray diffraction (XRD) was performed with a Rigaku D/MAX-RB X-ray

diffractometer by using Cu K $\alpha$  (40 kV, 40 mA) radiation and a secondary beam graphite monochromator. The morphologies were observed by a transmission electron microscope (TEM, JEM-200CX) and a field emission high resolution transmission electron microscope (HRTEM, JEM-2100F). Temperature-programmed reduction by hydrogen (H<sub>2</sub>-TPR) was obtained on a Tianjin XQ TP5080 autoadsorption apparatus. 80 mg of the calcined catalyst was outgassed at 300 °C under N<sub>2</sub> flow for 2 h. After cooling to room temperature under N<sub>2</sub> flow, the flowing gas was switched to 5% H<sub>2</sub>/N<sub>2</sub>, and the sample was heated to 950 °C at a ramping rate of 10 °C min<sup>-1</sup>. The H<sub>2</sub> consumption was monitored by a TCD. The laser Raman experiment was performed by using an inVia-reflex Renishaw spectrometer equipped with a holographic notch filter, a CCD detector, and a laser radiating at 514 nm. The surface properties were monitored from the FT-IR spectra recorded after the adsorption of pyridine, using a Bruker Vector 22 spectrometer coupled to a conventional high-vacuum system. The sample was compacted to a self-supporting wafer and calcined at 300 °C for 1 h in an in situ IR gas cell under vacuum before pyridine adsorption. Pyridine was adsorbed at room temperature. Then, the samples were heated to 100 °C and evacuated to remove the physisorbed and weakly chemisorbed pyridine. Temperature-programmed desorption of the adsorbed pyridine starting at 120 °C was studied by stepwise heating of the sample under a vacuum to characterize the types and strength of the acid sites. Difference spectra were obtained by subtracting the background (base spectrum) of the unloaded sample. The X-ray photoelectron spectroscopy (XPS) was recorded on a Perkin-Elmer PHI 5000C ESCA system equipped with a dual X-ray source, using the Mg K $\alpha$  (1253.6 eV) anode and a hemispherical energy analyzer. The background pressure during data acquisition was kept below 10<sup>-6</sup> Pa. All binding energies were calibrated using contaminant carbon (C1s = 284.6 eV) as a reference.

For more molecular details, the theoretical part was added into this work, aiming to understand the effect of MnO<sub>x</sub> on the Zr-Ce mixed oxide nanostructure. Thus, the simplified surface cluster was constructed on the {110} planes of the CeO<sub>2</sub> cluster model, the main planes found on ceria nanorods. In the calculations with periodic boundary conditions, the surface was represented by a thin slab with a vacuum gap of 10 Å. The MnO<sub>x</sub>-CeO<sub>2</sub>{110} was built by replacing one Ce atom with a Mn atom. The oxygen vacancy models for both CeO<sub>2</sub>{110} and MnO<sub>x</sub>-CeO<sub>2</sub>{110} were generated by removing one surface oxygen. All calculations were performed using the DMol<sup>3</sup> module of the Material Studio Program package (Accelrys Software Inc. Materials Studio Modeling, release 5.5, Accelrys Software Inc.: San Diego, CA, 2007). DFT of the double-numerical plus polarization function and GGA with PBE were used. The effective core potentials (ECP) and spin polarizations were applied. The Brillouin zone of the Monkhorst-Pack grid was set at 2 × 2 × 1, and the cutoff radius was assigned at 4.2 Å. The SCF convergence energy was set at 1 × 10<sup>-5</sup> Ha.

Furthermore, the NH<sub>3</sub> gas adsorption ability on different low index planes, {100}, {110}, and {111}, of CeO<sub>2</sub> was theoretically studied. Similarly, the calculations of molecular NH<sub>3</sub> adsorption on CeO<sub>2</sub>{100}, CeO<sub>2</sub>{110}, and CeO<sub>2</sub>{111} were carried out with the same method and basis function as used to optimize the MnO<sub>x</sub>-CeO<sub>2</sub>{110} surface oxide, but the SCF convergence energy was set at 1 × 10<sup>-4</sup> Ha to reduce the



time-consuming calculation. Full geometry relaxation of all surface–adsorbate structures was carried out.

**2.3. Catalytic Activity Measurements.** The SCR activity measurement was carried out in a fixed-bed quartz microreactor operating in a steady state flow mode. A 0.4 g portion of the catalysts was sieved with a 40–60 mesh and used in each test. The reactant gas composition was typically 550 ppm NO, 550 ppm NH<sub>3</sub>, 3% O<sub>2</sub>, 10% H<sub>2</sub>O (when used), and balance N<sub>2</sub>. The total flow rate was 250 mL/min, and thus, a gas hourly space velocity (GHSV) of 60 000 h<sup>−1</sup> was obtained. The temperature was increased from 120 to 300 °C. At each temperature step, the data were recorded when the SCR reaction reached steady state after 15 min. The concentration of NO in the inlet and outlet gases was measured by a KM9106 flue gas analyzer. The concentrations of N<sub>2</sub>O and NH<sub>3</sub> were measured by a Transmitter IR N<sub>2</sub>O analyzer and IQ350 ammonia analyzer.

### 3. RESULTS AND DISCUSSION

**3.1. Characteristics of Catalysts.** **3.1.1. Morphologies, Surface Area, and Phase Composition.** The TEM images, structural models, and EDS spectra of different MnO<sub>x</sub>/ZrO<sub>2</sub>–CeO<sub>2</sub> nanostructures are shown in Figure 1. The three different ZrO<sub>2</sub>–CeO<sub>2</sub> nanomaterials maintain their original crystal

shapes after the deposition of MnO<sub>x</sub>. Figure 1a shows that the MnZrCe-NR is composed of nanorods with a uniform diameter of  $11 \pm 3$  nm and a length within 15–90 nm. Figure 1b depicts the HRTEM image of MnZrCe-NR with a fast Fourier transform (FFT) analysis (inset). According to FFT analysis, two kinds of lattice fringe directions attributed to {110} and {100} were observed for the MnZrCe-NR, which have a respective interplanar spacing of 0.19 and 0.26 nm. Thus, the structural model of the MnZrCe-NR is shown in Figure 1c. It shows a 1D growth structure with a preferred growth direction along with {110}, and enclosed by {100} planes. These observations agree well with the previous report.<sup>21</sup> The TEM image of MnZrCe-NP (Figure 1e) reveals that they have a size of  $10.4 \pm 2.0$  nm. The HRTEM image of MnZrCe-NP in Figure 1f showed that two kinds of lattice fringe directions of {111} and {100} are observed with an interplanar spacing of 0.31 and 0.26 nm, respectively. The model of the MnZrCe-NP (Figure 1g) shows that the MnZrCe-NP is the truncated octahedra, enclosed by eight {111} and six {100} planes.<sup>17</sup> Figure 1i shows the MnZrCe-NC is a less uniform length within 100–200 nm. One kind of lattice fringe directions attributed to {100} planes was observed for the MnZrCe-NC in Figure 1j, which have an interplanar spacing of 0.26 nm. The MnZrCe-NC shows a cubic structure with growth directions along with {100} planes in Figure 1k, suggesting that the MnZrCe-NC only exposed {100} planes. The EDS spectra in Figure 1d, h, and l of the red circle region in panels b, f, and j confirm the presence of Zr and Mn elements, which indicates that the MnO<sub>x</sub> highly disperse on the surface over all the ZrO<sub>2</sub>–CeO<sub>2</sub> nanostructures. These observations indicate that the desired morphology of MnO<sub>x</sub>/ZrO<sub>2</sub>–CeO<sub>2</sub> nanostructures with different exposed planes is successfully synthesized.

The BET surface areas of the ZrCe-NR, ZrCe-NC, and ZrCe-NP are measured to be 111.2, 22.6, and 96.9 m<sup>2</sup> g<sup>−1</sup>, separately. After the deposition of MnO<sub>x</sub>, the BET areas of the MnZrCe-NR, MnZrCe-NC, and MnZrCe-NP decrease to 82.9, 20.4, and 65.2 m<sup>2</sup> g<sup>−1</sup>, respectively. The crystal structures of the different MnO<sub>x</sub>/ZrO<sub>2</sub>–CeO<sub>2</sub> nanostructures were investigated by XRD techniques and shown in Figure 2. The diffraction

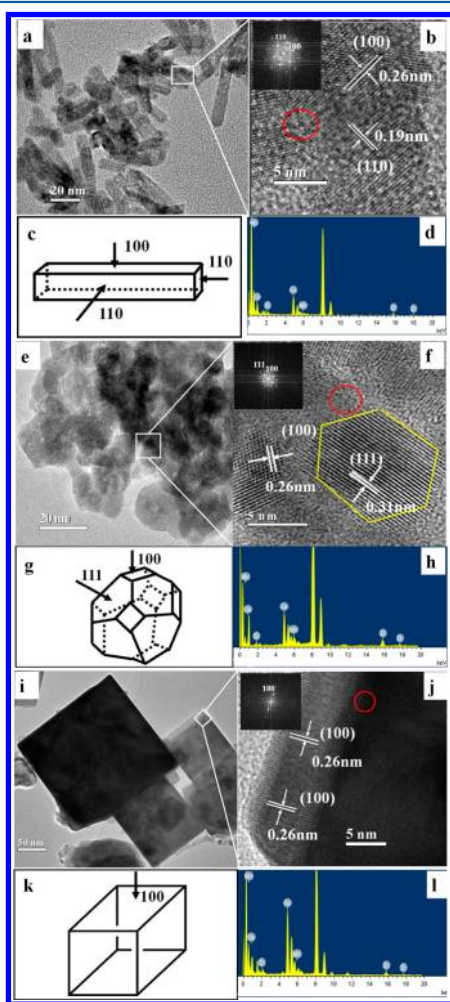


**Figure 1.** TEM and HRTEM images of MnZrCe-NR (a, b), MnZrCe-NR (e, f), and MnZrCe-NC (i, j); the structural model of MnZrCe-NR (c), MnZrCe-NR (g), and MnZrCe-NC (k); EDS patterns (d, h, l) of the red circle region in panels b, f, and j, respectively.

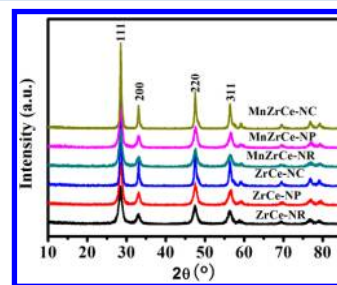


**Figure 2.** XRD patterns of ZrO<sub>2</sub>–CeO<sub>2</sub> and MnO<sub>x</sub>/ZrO<sub>2</sub>–CeO<sub>2</sub> nanostructures.

peaks at 28.5, 33.0, 47.5, 56.3, 59.1, 69.4, 76.8, and 79.1° could be ascribed to (111), (200), (220), (311), (222), (400), (331), and (420) of the face-centered cubic (fcc) structure of CeO<sub>2</sub> (JCPDS 43-1002). Interestingly, there are no peaks observed that are derived from the crystalline MnO<sub>x</sub> or ZrO<sub>2</sub>, which indicates a high dispersion of MnO<sub>x</sub> on the ZrO<sub>2</sub>–CeO<sub>2</sub> nanomaterials.

**3.1.2. Bulk and Surface Defects.** The visible Raman spectra of ZrO<sub>2</sub>–CeO<sub>2</sub> and MnO<sub>x</sub>/ZrO<sub>2</sub>–CeO<sub>2</sub> nanostructures are

compared in Figure 3. The Raman spectra of  $\text{ZrO}_2\text{--CeO}_2$  nanostructures (Figure 3a) show the distinct  $F_{2g}$  symmetry

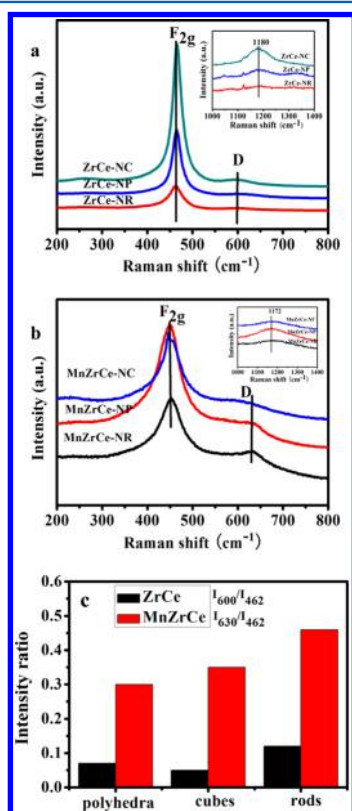


**Figure 3.** Raman spectra of  $\text{ZrO}_2\text{--CeO}_2$  (a) and  $\text{MnO}_x/\text{ZrO}_2\text{--CeO}_2$  (b) nanostructures and (c) the corresponding peak intensity ratios of  $I_{600}/I_{460}$  over  $\text{ZrO}_2\text{--CeO}_2$  and  $\text{MnO}_x/\text{ZrO}_2\text{--CeO}_2$  nanostructures.

mode of the  $\text{CeO}_2$  phase centered at about 462  $\text{cm}^{-1}$  with weak bands at 600 and 1180  $\text{cm}^{-1}$  due to the defect-induced (D) mode and the second-order longitudinal (2LO) mode, respectively.<sup>19,23,26</sup> The Raman spectra for  $\text{MnO}_x/\text{ZrO}_2\text{--CeO}_2$  nanostructures are similar to those of the supports (Figure 3b). The manganese oxide species led to the slight red shift of  $F_{2g}$  peaks from 462 to 450  $\text{cm}^{-1}$ . The peak at 600  $\text{cm}^{-1}$  for oxygen vacancies showed a blue shift to 630  $\text{cm}^{-1}$ , and the peak at 1180  $\text{cm}^{-1}$  shifted to 1172  $\text{cm}^{-1}$  and was remarkably broadened. We can attribute the observed shifts and broadening to the Mn incorporation in the lattice, demonstrating the influences of oxygen vacancies, phonon confinement, and inhomogeneous strain related to the presence of reduced states of cerium. These results further imply the incorporation of Mn ions into the surface/subsurface of ceria but without causing a change in the original cubic structure.

Importantly, the  $I_{600}/I_{462}$  values (Figure 3c), which indicate the defect concentration, such as oxygen vacancies, reached a maximum for  $\text{MnZrCe-NR}$ .  $\text{MnZrCe-NC}$  and  $\text{MnZrCe-NP}$  followed in sequence. After the incorporation of  $\text{MnO}_x$ , all of the intensity ratios increased sharply. Consequently, Mn ions showed a preference for insertion into the surface lattice of  $\text{CeO}_2$  and induced the increase of defect concentration in the  $\text{ZrO}_2\text{--CeO}_2$  nanostructures. In addition, the  $\text{MnZrCe-NR}$  displayed the highest value among them. This demonstrates that the interaction between manganese oxide and  $\text{ZrCe-NR}$  is stronger than that with  $\text{ZrCe-NC}$  and  $\text{ZrCe-NP}$ . Therefore, the

morphology of nanoscale ceria influences the synergistic interaction between  $\text{MnO}_x$  and  $\text{ZrO}_2\text{--CeO}_2$  nanostructures.

**3.1.3. Surface Properties.** The pyridine adsorption measured by IR spectroscopy was used to evaluate the strength and types of acid or basic sites of the  $\text{MnO}_x/\text{ZrO}_2\text{--CeO}_2$  nanostructures. Figure 4a shows the FT-IR spectra of  $\text{MnZrCe-NR}$  recorded

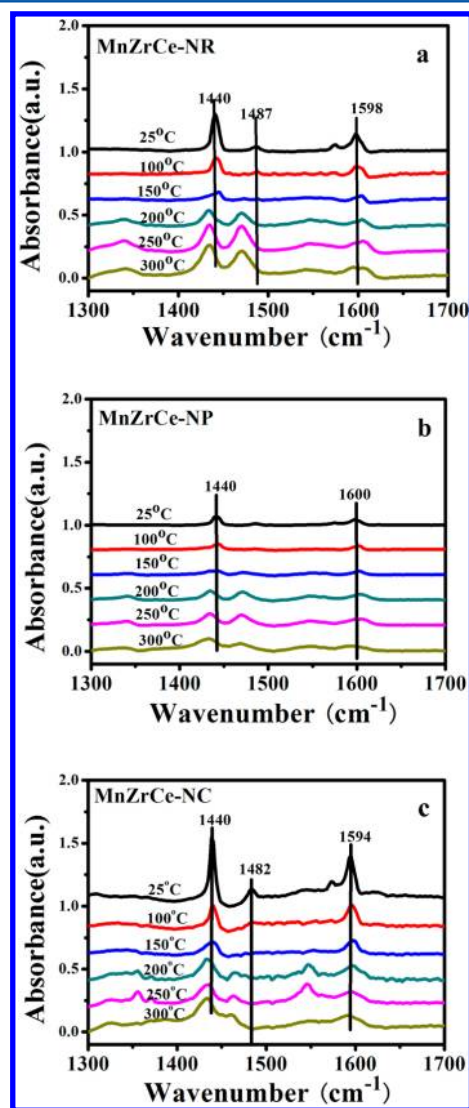


**Figure 4.** Py-IR spectra of  $\text{MnZrCe-NR}$  (a),  $\text{MnZrCe-NP}$  (b), and  $\text{MnZrCe-NC}$  (c).

after the adsorption of pyridine and subsequent evacuation at 25, 100, 150, 200, 250, and 300 °C. The Py-FT-IR spectrum at room temperature on the  $\text{MnZrCe-NR}$  sample shows bands at 1440 and 1598  $\text{cm}^{-1}$ , ascribed to pyridine coordinately bonded to weak surface Lewis acid sites,<sup>27,28</sup> and also shows weak bands at 1487  $\text{cm}^{-1}$  due to the protonated pyridine bonded to surface Brønsted acid sites,<sup>29</sup> indicating the presence of surface Brønsted acid sites. The intensities of all of these bands decrease and nearly vanish at 150 °C. There are new bands at 1433, 1471, and 1548  $\text{cm}^{-1}$  due to carboxylate and carbonaceous species<sup>30,31</sup> after outgassing above 200 °C, illustrating the existence of reactive basic  $\text{O}^{2-}$  species on  $\text{MnZrCe-NR}$  surfaces. The Py-FT-IR spectrum (Figure 4b) at room temperature on the  $\text{MnZrCe-NP}$  sample only shows weak bands at 1440 and 1598  $\text{cm}^{-1}$ , ascribed to weak surface Lewis acid sites. There are

also new bands at 1433, 1471, and 1548  $\text{cm}^{-1}$  after outgassing above 200  $^{\circ}\text{C}$ , while the intensities of these peaks are weaker than those of the MnZrCe-NR surfaces. The Py-FT-IR spectrum on the MnZrCe-NC sample shows the similar phenomenon with MnZrCe-NR. The bands at 1440, 1594, and 1482  $\text{cm}^{-1}$  are slightly stronger than those of the MnZrCe-NR, while the intensities of 1433, 1471, and 1548  $\text{cm}^{-1}$  are weaker than that of the MnZrCe-NR. These results indicate that at low temperature ( $<150$   $^{\circ}\text{C}$ ) the acid sites may be a key factor for the SCR activity, and the basic  $\text{O}^{2-}$  species may be another factor for the SCR activity at high temperature ( $\geq 200$   $^{\circ}\text{C}$ ).

**3.1.4. Redox Properties.** Figure 5 shows the  $\text{H}_2$ -TPR profiles of  $\text{ZrO}_2\text{--CeO}_2$  and  $\text{MnO}_x/\text{ZrO}_2\text{--CeO}_2$  nanostructures. All of

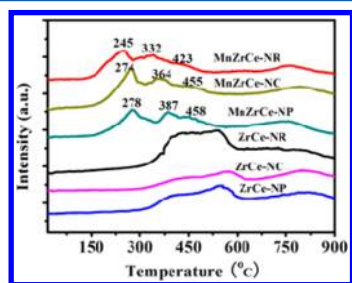


**Figure 5.**  $\text{H}_2$ -TPR profiles of  $\text{ZrO}_2\text{--CeO}_2$  and  $\text{MnO}_x/\text{ZrO}_2\text{--CeO}_2$  nanostructures.

the  $\text{ZrO}_2\text{--CeO}_2$  nanostructures showed broad peaks between 280 and 620  $^{\circ}\text{C}$ , while the  $\text{MnO}_x/\text{ZrO}_2\text{--CeO}_2$  nanostructures showed different profiles of the reduction peaks. The MnZrCe-NP showed three distinct reduction peaks. The peak at 278  $^{\circ}\text{C}$  represented the easy reduction of  $\text{MnO}_2$  to  $\text{Mn}_2\text{O}_3$ , and the peak at 387  $^{\circ}\text{C}$  was the further reduction of  $\text{Mn}_2\text{O}_3$  to  $\text{Mn}_3\text{O}_4$ , while the peak at 458  $^{\circ}\text{C}$  corresponded to the combined reductions of  $\text{Mn}_3\text{O}_4$  to  $\text{MnO}$  and surface  $\text{Ce}^{4+}$  to  $\text{Ce}^{3+}$  species.<sup>32</sup> A similar reduction profile was observed for the MnZrCe-NC, MnZrCe-NR, and MnZrCe-NP, except that the reduction peaks shifted to lower temperatures. These indicate that the interaction between  $\text{MnO}_x$  and  $\text{ZrCe-NR}$  is the strongest among the three catalysts. The stronger the interaction between  $\text{MnO}_x$  and  $\text{ZrO}_2\text{--CeO}_2$  nanostructures, the higher the oxidative ability of the  $\text{MnO}_x$  species.<sup>33</sup>

**3.1.5. Surface Composition, Chemical States, and Surface Oxygen Species.** The Mn 2p, Ce 3d, and O 1s XPS spectra of MnZrCe-NR, MnZrCe-NC, and MnZrCe-NP are given in Figure 6. By a peak-fitting deconvolution, the Mn  $2\text{P}_{3/2}$  spectra in Figure 6a can be separated into three peaks: 640.4, 641.9, or 642.0 and 644.6 eV, respectively. Qi et al.<sup>34</sup> and Chen et al.<sup>35</sup> have reported that the Mn  $2\text{P}_{3/2}$  binding energies of  $\text{Mn}^{2+}$ ,  $\text{Mn}^{3+}$ , and  $\text{Mn}^{4+}$  in the  $\text{MnO}_x\text{--CeO}_2$  mixed oxides were 640.3–640.7, 641.6–642.3, and 643.2–644.5 eV, separately. The concentrations of  $\text{Mn}^{2+}$ ,  $\text{Mn}^{3+}$ , and  $\text{Mn}^{4+}$  in MnZrCe-NR, MnZrCe-NC, and MnZrCe-NP are given in Table 1. The ratio of the higher valence state  $\text{Mn}^{4+}$  on the MnZrCe-NR is more than that on MnZrCe-NC and MnZrCe-NP.

The Ce 3d electron core level spectra of the MnZrCe-NR, MnZrCe-NC, and MnZrCe-NP are shown in Figure 6b. The  $\text{Ce}^{4+}$  has been fitted with six peaks:  $\nu_0$  ( $\sim 882.2$  eV),  $\nu_1$  ( $\sim 888.6$  eV),  $\nu_2$  ( $\sim 898$  eV),  $\nu_3$  ( $\sim 900.7$  eV),  $\nu_4$  ( $\sim 907.2$  eV), and  $\nu_5$  ( $\sim 916.15$  eV).  $\text{Ce}^{3+}$  has been fitted with four peaks:  $\mu_0$  ( $\sim 884.4$  eV),  $\mu_1$  ( $\sim 880.6$  eV),  $\mu_2$  ( $\sim 903.9$  eV), and  $\mu_3$  ( $\sim 899.3$  eV).<sup>36</sup> The surface concentrations of  $\text{Ce}^{3+}$  to the total Ce on the

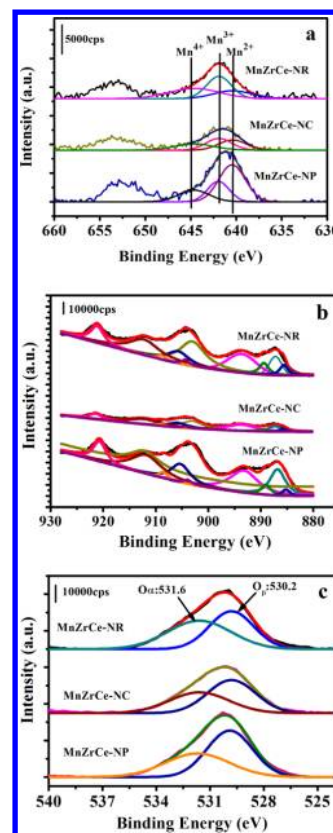


**Figure 6.** Mn 2p (a), Ce 3d (b), and O 1s (c) XPS spectra of  $\text{MnO}_x/\text{ZrO}_2\text{--CeO}_2$  nanostructures.

MnZrCe-NR, MnZrCe-NC, and MnZrCe-NP are 10.8, 7.5, and 7.2%, separately. Oxygen vacancies can be produced by the transformation between  $\text{Ce}^{3+}$  and  $\text{Ce}^{4+}$ ,  $4\text{Ce}^{4+} + \text{O}^{2-} \rightarrow 4\text{Ce}^{3+} + 2\text{e}^-/\square + 0.5\text{O}_2 \rightarrow 2\text{Ce}^{4+} + 4\text{Ce}^{3+} + \square + 0.5\text{O}_2$  (where  $\square$  represents an empty position).<sup>37</sup> The higher the  $\text{Ce}^{3+}$  concentration of the total Ce that exists, the more oxygen vacancies that form. This indicates that the oxygen vacancies of the MnZrCe-NR are more than those of MnZrCe-NC and MnZrCe-NP.

The O 1s bands of MnZrCe-NR, MnZrCe-NC, and MnZrCe-NP were shown in Figure 6c. The sub-bands at lower binding energy (529.6–530.0 eV) corresponded to the lattice oxygen  $\text{O}^{2-}$  (denoted as  $\text{O}_\beta$ ), and the sub-bands at higher binding energy (531.3–532.7 eV) corresponded to the surface adsorbed oxygen (denoted as  $\text{O}_\alpha$ ), such as  $\text{O}_2^{2-}$  or  $\text{O}^-$  belonging to defect oxide or hydroxyl-like group.<sup>38</sup> The quantitative peak-fitting results of O 1s can be seen in Table 1. The  $\text{O}_\alpha/\text{O}_\beta$  ratio of MnZrCe-NR is much higher than that of MnZrCe-NC and MnZrCe-NP, indicating the presence of abundant adsorbed surface oxygen on the MnZrCe-NR.

The optimized structures of the  $\text{CeO}_2\{110\}$  and  $\text{MnO}_x\text{--CeO}_2\{110\}$  surface models and their corresponding oxygen vacancy models are shown in Figure 7. The obtained results of distances and Mulliken charge distributions of the optimized  $\text{CeO}_2\{110\}$  and  $\text{MnO}_x\text{--CeO}_2\{110\}$  were listed in Table 2. For the  $\text{CeO}_2\{110\}$  surface, the Ce–O bond length was 2.315 Å, whereas, in the  $\text{MnO}_x\text{--CeO}_2\{110\}$  model, the Ce–O bond length increased to 2.481 Å and the Mn–O was 2.071 Å. Thus, the adjusted oxygen of manganese was closer to the Mn which led to the longer distance between Ce and O atoms; therefore, these affect the charge changes on Ce and O.



Table 1. Surface Chemical States and Quantitative Results of Samples Calculated from the XPS Data

| samples   | Mn <sup>a</sup> (%) | Ce <sup>a</sup> (%) | Zr <sup>a</sup> (%) | O <sup>a</sup> (%) | Mn <sup>b1</sup> (%) | Mn <sup>b2</sup> (%) | Mn <sup>b3</sup> (%) | Ce <sup>3+</sup> (%) | O <sub>s</sub> (%) |
|-----------|---------------------|---------------------|---------------------|--------------------|----------------------|----------------------|----------------------|----------------------|--------------------|
| MnZrCe-NR | 3.1                 | 17.6                | 3.3                 | 76.0               | 37.8                 | 40.2                 | 22.0                 | 10.8                 | 51.8               |
| MnZrCe-NC | 4.0                 | 7.6                 | 2.2                 | 86.2               | 29.5                 | 36.6                 | 33.9                 | 7.5                  | 43.6               |
| MnZrCe-NP | 4.2                 | 22.0                | 4.3                 | 69.5               | 20.3                 | 24.6                 | 55.1                 | 7.2                  | 41.8               |

<sup>a</sup>mol %. <sup>b</sup>b1 + b2 + b3 = 100%.

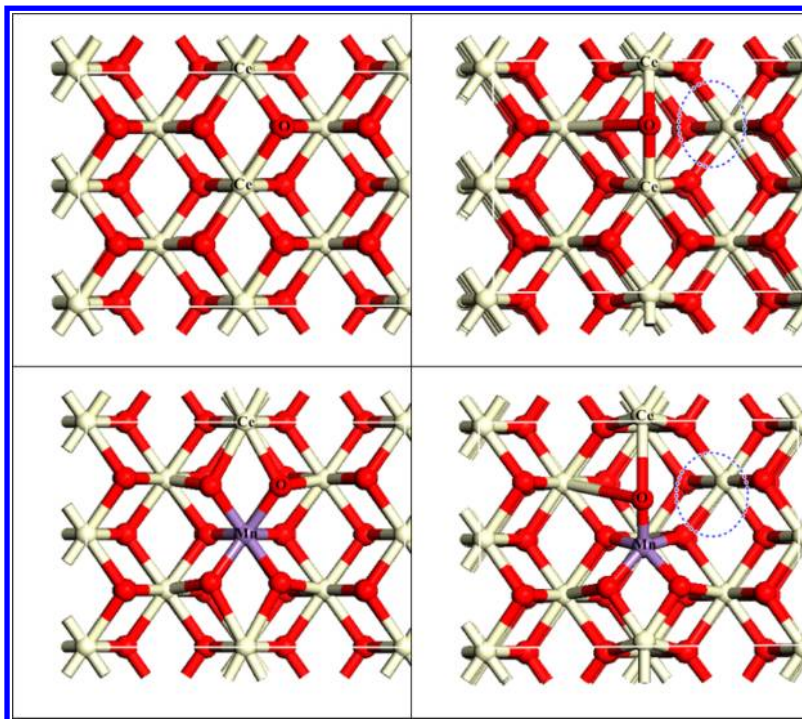


Figure 7. Model structures in top view of CeO<sub>2</sub>{110}, O-vacancy CeO<sub>2</sub>{110}, MnO<sub>x</sub>-CeO<sub>2</sub>{110}, and O-vacancy MnO<sub>x</sub>-CeO<sub>2</sub>{110}. The red, white, and purple colors represent oxygen, cerium, and manganese atoms, respectively.

Table 2. Selected Bond Distances and Mulliken Charges of CeO<sub>2</sub>{1 1 0} and MnO<sub>x</sub>-CeO<sub>2</sub>{1 1 0} Models

|  |      | bond distance (Å) |    | Mulliken charge (e <sup>-</sup> ) |
|--|------|-------------------|----|-----------------------------------|
| CeO <sub>2</sub> {1 1 0}                   | Ce-O | 2.315             | Ce | 1.521                             |
|  |      |                   | O  | -0.805                            |
| MnO <sub>x</sub> -CeO <sub>2</sub> {1 1 0} | Ce-O | 2.481             | Ce | 1.531                             |
|  |      |                   | O  | -0.683                            |
|  | Mn-O | 2.071             | O  | -0.683                            |

For the oxygen vacancy formation, a term of oxygen vacancy energy was used as the criteria to identify the oxygen vacancy feasibility, which was calculated from the different energy between the summation energy of the oxygen vacancy model and the  $\frac{1}{2}$  oxygen molecule, and the normal model of CeO<sub>2</sub>{110} or MnO<sub>x</sub>-CeO<sub>2</sub>{110}. The calculated energies of the oxygen vacancy of CeO<sub>2</sub>{110} and MnO<sub>x</sub>-CeO<sub>2</sub>{110} were 0.656 and -1.025 eV, respectively. The energy of the oxygen vacancy of the MnO<sub>x</sub>-CeO<sub>2</sub>{110} model was more negative than that of the normal CeO<sub>2</sub>{110} model, which can imply that the MnO<sub>x</sub> led to more facile oxygen vacancy formation on the surface of CeO<sub>2</sub>{110}, which is in good agreement with the Raman results.

**3.1.6. Characteristic of the Used Catalysts.** The morphologies of the used MnZrCe-NR, MnZrCe-NC, and MnZrCe-NP were observed by TEM images in Figure 8. The used MnZrCe-NR, MnZrCe-NC, and MnZrCe-NP still keep their shapes after the reaction, which indicated that the MnO<sub>x</sub>/ZrO<sub>2</sub>-CeO<sub>2</sub>

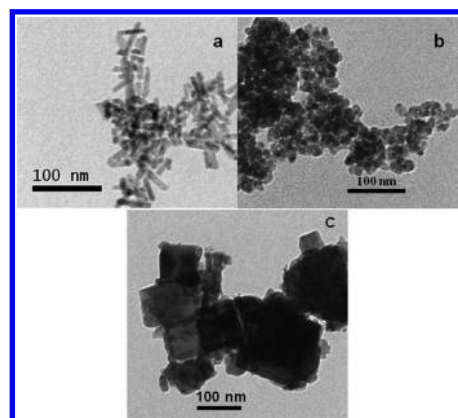


Figure 8. TEM images of the used catalysts: MnZrCe-NR (a), MnZrCe-NP (b), and MnZrCe-NC (c).

nanostructures had good structure stability during the SCR reaction.

The XRD patterns of the used MnO<sub>x</sub>/ZrO<sub>2</sub>-CeO<sub>2</sub> nanostructures have been shown in Figure 9. There are no peaks observed that are derived from the crystalline MnO<sub>x</sub> or ZrO<sub>2</sub> except for the diffraction peaks at 28.5, 33.0, 47.5, 56.3, 59.1, 69.4, 76.8, and 79.1° that could be ascribed to (111), (200), (220), (311), (222), (400), (331), and (420) of the face-centered cubic (fcc) structure of CeO<sub>2</sub> (JCPDS 43-1002), which indicates no crystalline MnO<sub>x</sub> forms after the SCR

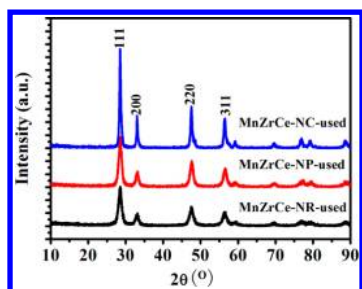


Figure 9. XRD patterns of the used  $\text{MnO}_x/\text{ZrO}_2\text{-CeO}_2$  nanostructures.

reaction. This also can explain that there is a strong interaction between  $\text{MnO}_x$  and  $\text{ZrO}_2\text{-CeO}_2$  nanomaterials which prevents the agglomeration of  $\text{MnO}_x$  during the SCR reaction.

**3.2. Catalytic Activity of Catalysts.** The catalytic activities of the  $\text{MnO}_x/\text{ZrO}_2\text{-CeO}_2$  nanostructures with different shapes are shown in Figure 10a. It is clear that the NO conversion over

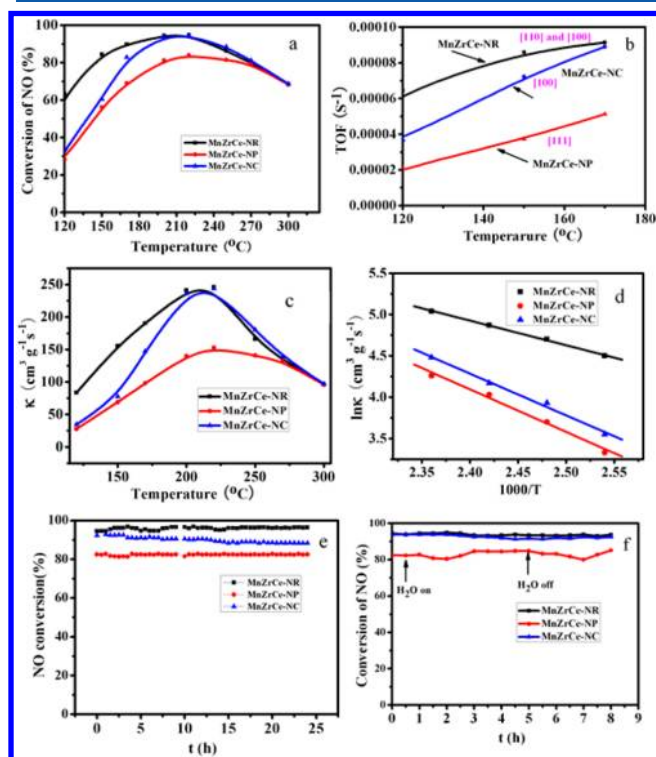


Figure 10. (a) NO conversion against temperature; (b) TOF profiles as a function of temperature; (c) temperature dependency of the first-order rate constant for  $\text{NH}_3\text{-SCR}$ ; (d) Arrhenius plots of the intrinsic reaction rate constants; and (e) long time stability tests over the  $\text{MnO}_x/\text{ZrO}_2\text{-CeO}_2$  nanostructures. (f) The effect of  $\text{H}_2\text{O}$  on NO conversion over  $\text{MnO}_x/\text{ZrO}_2\text{-CeO}_2$  nanostructures. Reaction conditions:  $250\text{ mL min}^{-1}$  total rate,  $550\text{ ppm NO}$ ,  $550\text{ ppm NH}_3$ ,  $3\%\text{ O}_2$ ,  $10\%\text{ H}_2\text{O}$  (when used), and  $\text{N}_2$  balance,  $200\text{ }^\circ\text{C}$ , and GHSV =  $60\,000\text{ h}^{-1}$ .

all of the catalysts increases first and then decreases with the temperature rising. A significant difference on the catalytic activity was observed. The  $\text{MnZrCe-NR}$  displays the highest NO conversion and the most extensive operating-temperature window among the three catalysts, followed by the  $\text{MnZrCe-NC}$ , and the  $\text{MnZrCe-NP}$  are the least active. Since the three nanoshapes have well-defined exposed surface planes, it is possible to compare the NO reduction activity on the basis of

surface oxygen sites. The NO turnover frequency (TOF) over the three catalysts with the different temperatures is compared in Figure 10b. The relative TOF ( $\text{s}^{-1}$ ) of NO over  $\text{MnO}_x$  species was calculated by the following equation:

$$\text{TOF} = \frac{(P\nu/RT)X_{\text{NO}}}{m_{\text{cat}}\beta_{\text{Mn}}/M_{\text{Mn}}} \quad (1)$$

where  $P$  is the standard atmospheric pressure ( $1.01 \times 10^5\text{ Pa}$ ),  $\nu$  is the flow rate of NO ( $1.0\text{ mL min}^{-1}$ ),  $R$  is the proportional constant ( $8.314\text{ J mol}^{-1}\text{ K}^{-1}$ ),  $T$  is the temperature (K),  $X_{\text{NO}}$  is the NO conversion of the catalyst (%),  $m_{\text{cat}}$  is the mass of the catalyst (0.4 g),  $\beta_{\text{Mn}}$  is the Mn loading calculated from the XPS spectra (%), and  $M_{\text{Mn}}$  is the molar mass of Mn ( $54.94\text{ g mol}^{-1}$ ).

On the basis of the NO conversion at different temperatures, the TOFs for the (a)  $\text{MnZrCe-NR}$ , (b)  $\text{MnZrCe-NP}$ , and (c)  $\text{MnZrCe-NC}$  catalysts were calculated using the above equation. Similar to the activity profiles, the TOF of NO over  $\text{MnZrCe-NR}$  is higher than  $\text{MnZrCe-NC}$ , and that of  $\text{MnZrCe-NP}$  is the least one. The  $\text{MnZrCe-NR}$  catalyst has {110} and {100} planes, the  $\text{MnZrCe-NC}$  catalyst has {100} planes, and  $\text{MnZrCe-NP}$  has {111} planes. Thus, the structure dependence of NO reduction over the three catalysts is clearly demonstrated, {110} and {100} planes > {100} planes > {111} planes.

The  $\text{NH}_3$  gas adsorption over the three types of low index  $\text{CeO}_2$  models, {100}, {110}, and {111}, was theoretically studied. The optimized structures of  $\text{NH}_3$  gas over  $\text{CeO}_2\{100\}$ ,  $\text{CeO}_2\{110\}$ , and  $\text{CeO}_2\{111\}$  were shown in Figure S1 (Supporting Information). The adsorption energy ( $E_d$ ) is defined as follows:

$$E_d = E_{\text{surface}+\text{NH}_3} - E_{\text{surface}} - E_{\text{NH}_3} \quad (2)$$

where  $E_{\text{surface}+\text{NH}_3}$  means the optimized energy of the  $\text{NH}_3$  gas adsorbate–surface system and  $E_{\text{surface}}$  and  $E_{\text{NH}_3}$  are the naked energies of surface and  $\text{NH}_3$  gas, respectively.

Therefore, more negative  $E_d$  values mean more attractive adsorption energies, whereas the positive values are more repulsive adsorption energies. The obtained  $\text{NH}_3$  gas adsorption energies over  $\text{CeO}_2\{100\}$ ,  $\text{CeO}_2\{110\}$ , and  $\text{CeO}_2\{111\}$  are listed in Table 3. The  $\text{CeO}_2\{110\}$  surface

Table 3.  $\text{NH}_3$  Gas Adsorption Energies over the  $\text{CeO}_2\{100\}$ ,  $\{110\}$ , and  $\{111\}$  Models

| system                | $\text{NH}_3$ adsorption energy (eV) | adsorption distance ( $\text{\AA}$ ) |
|-----------------------|--------------------------------------|--------------------------------------|
| $\text{CeO}_2\{110\}$ | −1.411                               | 2.760                                |
| $\text{CeO}_2\{100\}$ | −1.002                               | 2.856                                |
| $\text{CeO}_2\{111\}$ | −0.659                               | 2.671                                |

model shows the best adsorption energy of about −1.411 eV with interaction distance from Ce to the N atom of  $\text{NH}_3$  at 2.760  $\text{\AA}$ . Consequently, the  $\text{CeO}_2\{100\}$  model gives the second adsorption energy with −1.002 eV and the adsorbed distance of  $\text{NH}_3$  on the top of Ce is 2.856  $\text{\AA}$  which is longer than the  $\text{CeO}_2\{110\}$  model. For the  $\text{CeO}_2\{111\}$  model results in the closest  $\text{NH}_3$  gas adsorbed distance interaction but gives the lowest  $\text{NH}_3$  adsorption energy at −0.659 eV. The  $\text{CeO}_2\{111\}$  structure has been reported that it was the highest surface stability; therefore, the  $\text{NH}_3$  adsorption reactivity is the smallest one.

To understand the intrinsic effect of the morphology of  $\text{ZrO}_2\text{-CeO}_2$  nanostructures on the  $\text{MnO}_x/\text{ZrO}_2\text{-CeO}_2$



Table 4. Performance of Various Catalysts for the NH<sub>3</sub>-SCR of NO

| catalyst  | NO (ppm) | NH <sub>3</sub> (ppm) | O <sub>2</sub> (%) | <i>t</i> (°C) | <i>X</i> <sub>NO</sub> <sup>a</sup> | <i>κ</i> <sup>b</sup> (cm <sup>3</sup> g <sup>-1</sup> s <sup>-1</sup> ) |
|---|----------|-----------------------|--------------------|---------------|-------------------------------------|--|
| MnZrCe-NR   | 550      | 550                   | 3                  | 120           | 63.4                                | 83.4   |
| MnZrCe-NC   | 550      | 550                   | 3                  | 120           | 33.9                                | 34.9   |
| MnZrCe-NP   | 550      | 550                   | 2                  | 120           | 28.3                                | 28.0   |
| MnO <sub>x</sub> (0.4)–CeO <sub>2</sub> (500) <sup>11</sup>                     | 1000     | 1000                  | 2                  | 120           | 65                                  | 23.4   |
| MnO <sub>x</sub> (0.4)–Zr(0.1)–CeO <sub>2</sub> (500) <sup>11</sup>             | 1000     | 1000                  | 2                  | 120           | 70                                  | 26.8   |
| MnO <sub>x</sub> (0.3)–CeO <sub>2</sub> (650) <sup>10</sup>                     | 1000     | 1000                  | 2                  | 120           | 75                                  | 76.17  |
| V <sub>2</sub> O <sub>5</sub> –WO <sub>3</sub> /TiO <sub>2</sub> <sup>2</sup>   | 1000     | 1000                  | 2                  | 450           | 69                                  | 78.9   |
| MnNaY775 <sup>40</sup>  | 1000     | 1000                  | 2                  | 150           | 82                                  | 13.33  |
| V <sub>2</sub> O <sub>5</sub> /AC <sup>41</sup>                                 | 500      | 560                   | 3.3                | 250           | 79.7                                | 69.96  |
| V <sub>2</sub> O <sub>5</sub> /CeO <sub>2</sub> –ZrO <sub>2</sub> <sup>25</sup> | 1000     | 1100                  | 3.5                | 220           |                                     | 50   |

<sup>a</sup>NO conversion. <sup>b</sup>First-order rate constant.

catalysts, the catalytic performance data are analyzed by the macro-kinetic approach. The NH<sub>3</sub>-SCR on the MnO<sub>x</sub>–CeO<sub>2</sub> was generally considered to be a first-order reaction with respect to NO.<sup>10,11</sup> Assuming the diffusion-limitation free, the effective first-order rate constant is related to NO conversion (*X*) by

$$\kappa = -\frac{F_0}{[\text{NO}]_0 W_{\text{cat}}} \ln(1 - X) \quad (3)$$

$$\kappa = A \exp(-E_a/RT) \quad (4)$$

where  $\kappa$  is the reaction constant (cm<sup>3</sup> g<sup>-1</sup> s<sup>-1</sup>),  $F_0$  is the molar NO feed rate (mol s<sup>-1</sup>),  $[\text{NO}]_0$  is the molar NO concentration at the inlet (mol cm<sup>-3</sup>),  $W_{\text{cat}}$  is the catalyst weight (g), *X* is the conversion of NO (%), *A* is the pre-exponential factor,  $E_a$  is the apparent activation energy (kJ mol<sup>-1</sup>), *R* is the gas constant (8.3145 J mol<sup>-1</sup> K<sup>-1</sup>), and *T* is the temperature (K).

The temperature dependency of first-order rate constant for NH<sub>3</sub>-SCR over the MnO<sub>x</sub>/ZrO<sub>2</sub>–CeO<sub>2</sub> nanostructures is shown in Figure 10c. The MnZrCe-NR is more active than MnZrCe-NC and MnZrCe-NP. From the XPS results, the ratio of the higher valence state Mn<sup>4+</sup> on the MnZrCe-NR is more than that on MnZrCe-NC and MnZrCe-NP. It has been reported that, with increasing Mn<sup>4+</sup>/Mn<sup>3+</sup> ratio, the oxidation of NO to NO<sub>2</sub> would get enhanced,<sup>7,39</sup> which is beneficial to the low temperature SCR activity. Hence, it can be concluded that the Mn<sup>4+</sup> must play an important role in this SCR process. On the other hand, there are more oxide defects and adsorbed surface oxygen on the MnZrCe-NR catalyst. The surface oxygen which can absorb an active gaseous O<sub>2</sub> to form active oxygen species is more reactive in oxidation reactions due to its high mobility than lattice oxygen oxygen O<sub>β</sub>, which might be beneficial for the enhancement of NO oxidation and thus the SCR activity.<sup>14,31</sup> A summary comparison has been made for the MnO<sub>x</sub>/ZrO<sub>2</sub>–CeO<sub>2</sub> nanostructures with other high-activity catalysts that were reported in the literature in Table 4. The MnZrCe-NR catalyst is more active than all other catalysts.<sup>10,11,40,41</sup>

Figure 10d shows the Arrhenius plots based on the reaction rate data between 120 and 140 °C. The pre-exponential factor and apparent activation energy are determined from these plots based on eq 4 and given in Table 5. On the MnZrCe-NR catalyst, the apparent activation energy is 25 kJ mol<sup>-1</sup>, which was much lower than the values of MnZrCe-NC and MnZrCe-NP catalysts (42 and 43 kJ mol<sup>-1</sup>). Therefore, the catalytic activity of MnZrCe-NR catalyst was higher than that of the MnZrCe-NC and MnZrCe-NP catalysts. Compared with the references,<sup>42,43</sup> the MnZrCe-NR catalyst also needs less energy

Table 5. Kinetic Parameter Comparison of the MnO<sub>x</sub>/ZrO<sub>2</sub>–CeO<sub>2</sub> Nanostructures

| sample    | <i>A</i>              | <i>E<sub>a</sub></i> (kJ mol <sup>-1</sup> ) |
|-----------|-----------------------|--|
| MnZrCe-NR | 1.8 × 10 <sup>6</sup> | 25   |
| MnZrCe-NC | 1.3 × 10 <sup>7</sup> | 42   |
| MnZrCe-NP | 1.4 × 10 <sup>7</sup> | 43   |

for the reaction, resulting in the excellent catalytic performance. From the above characterization, MnZrCe-NR catalyst has {110} and {100} planes, MnZrCe-NC catalyst has {100} planes, and MnZrCe-NP has {111} and {100} planes. The oxidative ability, interaction between MnO<sub>x</sub> and ZrCe-NR, adsorbed surface oxygen, and oxygen vacancies are dependent on the exposed planes which are determined by the morphology of the ZrO<sub>2</sub>–CeO<sub>2</sub> nanostructures. The MnZrCe-NR catalyst with the higher oxidative ability, the stronger interaction between MnO<sub>x</sub> and ZrCe-NR, the more adsorbed surface oxygen, and more oxygen vacancies is more active than the other catalysts. The relationship between the SCR performance and structure of the three catalysts is clearly demonstrated, and the sequence of the active planes is {110} planes > {100} planes > {111} planes.

The long time stability tests of MnO<sub>x</sub>/ZrO<sub>2</sub>–CeO<sub>2</sub> nanostructures with different shapes are shown in Figure 10e. It is examined under the following reaction conditions: 550 ppm NO, 550 ppm NH<sub>3</sub>, 3% O<sub>2</sub>, 200 °C, and GHSV of 60 000 h<sup>-1</sup>. From Figure 10c, the MnZrCe-NR catalyst shows good stability after 24 h. It is well-known that the deactivation of the Mn-based catalysts for the SCR mainly results from the sintering of active MnO<sub>x</sub>.<sup>44</sup> From the XRD analysis of the catalysts after reaction, we can find that there is no crystalline MnO<sub>x</sub> on the MnZrCe-NR catalysts used. Therefore, it can be concluded that there is a strong interaction between MnO<sub>x</sub> and ZrCe-NR. Meanwhile, the other two catalysts also show good stability. The resistance to H<sub>2</sub>O of MnO<sub>x</sub>/ZrO<sub>2</sub>–CeO<sub>2</sub> nanostructures is shown in Figure 10f. It is clear that all MnO<sub>x</sub>/ZrO<sub>2</sub>–CeO<sub>2</sub> nanostructures show good resistance to H<sub>2</sub>O.

On the basis of the earlier reports<sup>34,45–50</sup> and our experiment results, the SCR reaction mechanism of NO with NH<sub>3</sub> on the MnZrCe-NR catalyst is proposed. The NO molecules are first adsorbed on the adsorbed surface oxygen and then oxidized to NO<sub>2</sub> and form an oxygen vacancy. The NH<sub>3</sub> molecules adsorbed on MnO<sub>x</sub> form coordinated NH<sub>3</sub> and NH<sub>2</sub>. Then, the adsorbed NH<sub>3</sub> and NO<sub>2</sub> react to form H<sub>2</sub>O and N<sub>2</sub>. On the other hand, the adsorbed NH<sub>2</sub> and gas NO react to form NH<sub>2</sub>NO which is not stable and then dissociate to H<sub>2</sub>O and N<sub>2</sub>.

Then, the gaseous  $O_2$  is adsorbed to oxidize the oxygen vacancies to form active oxygen species. The  $NH_3$  gas adsorption over the three types of low index  $CeO_2$  structures {100}, {110}, and {111} agrees well with the experimental results that the Zr- $CeO_2$  nanorod shape having the dominant low index on {110} planes showed the best SCR catalytic activity. The exposed {110} and {100} planes of ZrCe-NR have more oxygen vacancies, which indicates that active oxygen species formed on the MnZrCe-NR are more during the SCR reaction. According to Qi et al.,<sup>34</sup> the higher activity of the  $MnO_x$ - $CeO_2$  catalysts is attributed to the highly dispersed Mn species and more active oxygen species.

#### 4. CONCLUSIONS

The  $MnO_x/ZrO_2$ - $CeO_2$  nanorods achieved significantly higher NO conversions than the nanocubes and nanopolyhedra in the  $NH_3$ -SCR of NO. The  $MnO_x/ZrO_2$ - $CeO_2$  nanorods also achieved a significantly higher rate constant with respect to NO conversion than that of nanocubes and nanopolyhedra. On the nanorods, the apparent activation energy is  $25\text{ kJ mol}^{-1}$ , which was much lower than the values of nanocubes and nanopolyhedra (42 and  $43\text{ kJ mol}^{-1}$ ). The HRTEM images reveal that the  $MnO_x/ZrO_2$ - $CeO_2$  nanorods predominately expose {110} and {100} planes. From the XPS and Raman results, it can be concluded that the Mn, Ce valences, surface oxygen species, and oxygen vacancies show the morphology dependence. The excellent catalytic activity of the  $MnO_x/ZrO_2$ - $CeO_2$  nanorods should be attributed to the abundant  $Mn^{4+}$  species, adsorbed surface oxygen, and oxygen vacancies which are associated with their exposed {110} and {100} planes. The long time stability of  $MnO_x/ZrO_2$ - $CeO_2$  nanorods confirmed that these materials could be considered as excellent catalysts for the low temperature SCR of NO with ammonia. This work indicates that designing better performing catalytic materials could be realized through the shape-selective synthesis.

#### ■ ASSOCIATED CONTENT

##### Supporting Information

The optimized structures of  $NH_3$  gas over  $CeO_2\{100\}$ ,  $CeO_2\{110\}$ , and  $CeO_2\{111\}$ . This material is available free of charge via the Internet at <http://pubs.acs.org>.

#### ■ AUTHOR INFORMATION

##### Corresponding Author

\*Phone: +86-21-66136081. Fax: +86-21-66136079. E-mail: dszhang@shu.edu.cn (D.Z.); shiliyi@shu.edu.cn (L.S.).

##### Notes

The authors declare no competing financial interest.

#### ■ ACKNOWLEDGMENTS

The authors acknowledge the support of National Natural Science Foundation of China (51108258), Science and Technology Commission of Shanghai Municipality (10540500100 and 11nm0502200), Doctoral Fund of Ministry of Education of China (20123108120018), Research Fund for the innovation Program of Shanghai University (A.10040711003), and Shanghai Municipal Education Commission (B.37040711001). P.M. acknowledges the support of the STCSM postdoctoral foundation (12R21413300). The authors would like to thank Mr. Y. L. Chu and Mr. W. J. Yu for help with the SEM and TEM measurements. We thank Thai

Government Stimulus Package 2 (TKK2555) for computing resources.

#### ■ REFERENCES

- (1) Jung, S. M.; Grange, P. Characterization and Reactivity of  $V_2O_5$ - $WO_3$  Supported on  $TiO_2$ - $SO_4^{2-}$  Catalyst for the SCR Reaction. *Appl. Catal., B* **2001**, 32, 123–131.
- (2) Long, R. Q.; Yang, R. T. Selective Catalytic Reduction of NO with Ammonia over  $V_2O_5$  Doped  $TiO_2$  Pillared Clay Catalysts. *Appl. Catal., B* **2000**, 24, 13–21.
- (3) Chae, H. J.; Nam, I. S.; Ham, S. W.; Hong, S. B. Characteristics of Vanadia on the Surface of  $V_2O_5/Ti$ -PILC Catalyst for the Reduction of  $NO_x$  by  $NH_3$ . *Appl. Catal., B* **2004**, 53, 117–126.
- (4) Shen, B. X.; Liu, T.; Zhao, N.; Yang, X. Y.; Deng, L. D. Iron-Doped Mn-Ce/ $TiO_2$  Catalyst for Low Temperature Selective Catalytic Reduction of NO with  $NH_3$ . *J. Environ. Sci. (Beijing, China)* **2010**, 22, 1447–1454.
- (5) Kim, Y. J.; Kwon, H. J.; Nam, I. S.; Choung, J. W.; Kil, J. K.; Kim, H. J.; Cha, M. S.; Yeo, G. K. High de $NO_x$  Performance of Mn/ $TiO_2$  Catalyst by  $NH_3$ . *Catal. Today* **2010**, 151, 244–250.
- (6) Kang, M.; Park, E. D.; Kim, J. M.; Yie, J. E. Cu-Mn Mixed Oxides for Low Temperature NO Reduction with  $NH_3$ . *Catal. Today* **2006**, 111, 236–241.
- (7) Kang, M.; Park, E. D.; Kim, J. M.; Yie, J. E. Manganese Oxide Catalysts for  $NO_x$  Reduction with  $NH_3$  at Low Temperatures. *Appl. Catal., A* **2007**, 327, 261–269.
- (8) Xu, H. D.; Qiu, C. T.; Zhang, Q. L.; Lin, T.; Gong, M. C.; Chen, Y. Q. Influence of Tungsten Oxide on Selective Catalytic Reduction of  $NO_x$  with  $NH_3$  over  $MnO_x$ - $CeO_2$  / $ZrO_2$ - $TiO_2$  Monolith Catalyst. *Acta Phys.-Chim. Sin.* **2010**, 26, 2449–2454.
- (9) Maitarad, P.; Zhang, D. S.; Gao, R. H.; Shi, L. Y.; Li, H. R.; Huang, L.; Rungtongmongkol, T.; Zhang, J. P. Combination of Experimental and Theoretical Investigations of  $MnO_x/Ce_{0.9}Zr_{0.1}O_2$  Nanorods for Selective Catalytic Reduction of NO with Ammonia. *J. Phys. Chem. C* **2013**, DOI: 10.1021/jp400504m.
- (10) Qi, G. S.; Yang, R. T. Performance and Kinetics Study for Low-Temperature SCR of NO with  $NH_3$  over  $MnO_x$ - $CeO_2$  Catalyst. *J. Catal.* **2003**, 217, 434–441.
- (11) Qi, G. S.; Yang, R. T.; Chang, R.  $MnO_x$ - $CeO_2$  Mixed Oxides Prepared by Co-Precipitation for Selective Catalytic Reduction of NO with  $NH_3$  at Low Temperatures. *Appl. Catal., B* **2004**, 51, 93–106.
- (12) Wu, Z. B.; Jin, R. B.; Wang, H. Q.; Liu, Y. Effect of Ceria Doping on  $SO_2$  Resistance of Mn/ $TiO_2$  for Selective Catalytic Reduction of NO with  $NH_3$  at Low Temperature. *Catal. Commun.* **2009**, 10, 935–939.
- (13) Jin, R.; Liu, Y.; Wu, Z.; Wang, H.; Gu, T. Relationship between  $SO_2$  Poisoning Effects and Reaction Temperature for Selective Catalytic Reduction of NO over Mn-Ce/ $TiO_2$  Catalyst. *Catal. Today* **2010**, 153, 84–89.
- (14) Zhang, D. S.; Du, X. J.; Shi, L. Y.; Gao, R. H. Shape-Controlled Synthesis and Catalytic Application of Ceria Nanomaterials. *Dalton Trans.* **2012**, 41, 14455–14475.
- (15) Du, N.; Zhang, H.; Chen, B. G.; Ma, X. Y.; Yang, D. R. Ligand-Free Self-Assembly of Ceria Nanocrystals into Nanorods by Oriented Attachment at Low Temperature. *J. Phys. Chem. C* **2007**, 111, 12677–12680.
- (16) Mai, H. X.; Sun, L. D.; Zhang, Y. W.; Si, R.; Feng, W.; Zhang, H. P.; Liu, H. C.; Yan, C. H. Shape-Selective Synthesis and Oxygen Storage Behavior of Ceria Nanopolyhedra, Nanorods, and Nanocubes. *J. Phys. Chem. B* **2005**, 109, 24380–24385.
- (17) Wang, Z. L.; Feng, X. D. Polyhedral Shapes of  $CeO_2$  Nanoparticles. *J. Phys. Chem. B* **2003**, 107, 13563–13566.
- (18) Sayle, T. H.; Parker, S. C.; Sayle, D. C. Oxidising CO to  $CO_2$  Using Ceria Nanoparticles. *Phys. Chem. Chem. Phys.* **2005**, 7, 2936–2941.
- (19) Liu, L. J.; Yao, Z. J.; Deng, Y.; Gao, F.; Liu, B.; Dong, L. Morphology and Crystal-Plane Effects of Nanoscale Ceria on the Activity of  $CuO/CeO_2$  for NO Reduction by CO. *ChemCatChem* **2011**, 3, 978–989.

- (20) Gawade, P.; Mirkelamoglu, B.; Ozkan, U. S. The Role of Support Morphology and Impregnation Medium on the Water Gas Shift Activity of Ceria-Supported Copper Catalysts. *J. Phys. Chem. C* **2010**, *114*, 18173–18181.
- (21) Zhou, K.; Wang, X.; Sun, X.; Peng, Q.; Li, Y. Enhanced Catalytic Activity of Ceria Nanorods from Well-Defined Reactive Crystal Planes. *J. Catal.* **2005**, *229*, 206–212.
- (22) Wu, Z.; Li, M.; Overbury, S. H. On the Structure Dependence of CO Oxidation over CeO<sub>2</sub> Nanocrystals with Well-Defined Surface. *J. Catal.* **2012**, *285*, 61–73.
- (23) Du, X. J.; Zhang, D. S.; Shi, L. Y.; Gao, R. H.; Zhang, J. P. Morphology Dependence of Catalytic Properties of Ni/CeO<sub>2</sub> Nanostructures for Carbon Dioxide Reforming of Methane. *J. Phys. Chem. C* **2012**, *116*, 10009–10016.
- (24) Li, Y.; Cheng, H.; Li, D. Y.; Qin, Y. S.; Xie, Y. M.; Wang, S. D. WO<sub>3</sub>/CeO<sub>2</sub>-ZrO<sub>2</sub>, a Promising Catalyst for Selective Catalytic Reduction (SCR) of NO<sub>x</sub> with NH<sub>3</sub> in Diesel Exhaust. *Chem. Commun.* **2008**, 1470–1472.
- (25) Putluru, S. S. R.; Riisager, A.; Fehrmann, R. The Effect of Acidic and Redox Properties of V<sub>2</sub>O<sub>5</sub>/CeO<sub>2</sub>-ZrO<sub>2</sub> Catalysts in Selective Catalytic Reduction of NO by NH<sub>3</sub>. *Catal. Lett.* **2009**, *133*, 370–375.
- (26) Wu, Z.; Li, M.; Howe, J.; Meyer, H. M.; Overbury, S. H. Probing Defect Sites on CeO<sub>2</sub> Nanocrystals with Well-Defined Surface Planes by Raman Spectroscopy and O<sub>2</sub> Adsorption. *Langmuir* **2010**, *26*, 16595–16606.
- (27) Martin, C.; Malet, P.; Solana, G.; Rives, V. Structural Analysis of Silica-Supported Tungstates. *J. Phys. Chem. B* **1998**, *102*, 2759–2768.
- (28) Lin, Q. C.; Li, J. H.; Ma, L.; Hao, J. M. Selective Catalytic Reduction of NO with NH<sub>3</sub> over Mn–Fe/USY under Lean Burn Conditions. *Catal. Today* **2010**, *151*, 251–256.
- (29) Wachs, I. E. Raman and IR Studies of Surface Metal Oxide Species on Oxide Supports: Supported Metal Oxide Catalysts. *Catal. Today* **1996**, *27*, 437–455.
- (30) Zaki, M. I.; Hasan, M. A.; Al-Sagheer, F. A.; Pasupulety, L. In Situ FTIR Spectra of Pyridine Adsorbed on SiO<sub>2</sub>-Al<sub>2</sub>O<sub>3</sub>/TiO<sub>2</sub>, ZrO<sub>2</sub> and CeO<sub>2</sub>: General Considerations for the Identification of Acid Sites on Surfaces of Finely Divided Metal Oxides. *Colloids Surf., A* **2001**, *190*, 261–274.
- (31) Zaki, M. I.; Hasan, M. A.; Pasupulety, L. Surface Reactions of Acetone on Al<sub>2</sub>O<sub>3</sub>, TiO<sub>2</sub>, ZrO<sub>2</sub>, and CeO<sub>2</sub>: IR Spectroscopic Assessment of Impacts of the Surface Acid-Base Properties. *Langmuir* **2001**, *17*, 768–774.
- (32) Zhang, Q.; Qiu, C.; Xu, H.; Lin, T.; Lin, Z.; Gong, M.; Chen, Y. Low-Temperature Selective Catalytic Reduction of NO with NH<sub>3</sub> over Monolith Catalyst of MnO<sub>x</sub>/CeO<sub>2</sub>-ZrO<sub>2</sub>-Al<sub>2</sub>O<sub>3</sub>. *Catal. Today* **2011**, *175*, 171–176.
- (33) Gupta, A.; Waghmare, U. V.; Hegde, M. S. Correlation of Oxygen Storage Capacity and Structural Distortion in Transition-Metal-, Noble-Metal-, and Rare-Earth-Ion-Substituted CeO<sub>2</sub> from First Principles Calculation. *Chem. Mater.* **2010**, *22*, 5184–5198.
- (34) Qi, G. S.; Yang, R. T. Characterization and FTIR Studies of MnO<sub>x</sub>-CeO<sub>2</sub> Catalyst for Low-Temperature Selective Catalytic Reduction of NO with NH<sub>3</sub>. *J. Phys. Chem. B* **2004**, *108*, 15738–15747.
- (35) Chen, Z. H.; Yang, Q.; Li, H.; Li, X. H.; Wang, L. F.; Tsang, S. C. Cr–MnO<sub>x</sub> Mixed-Oxide Catalysts for Selective Catalytic Reduction of NO<sub>x</sub> with NH<sub>3</sub> at Low Temperature. *J. Catal.* **2010**, *276*, 56–65.
- (36) Larachi, F.; Pierre, J.; Adnot, A.; Bernis, A. Ce 3d XPS Study of Composite Ce<sub>x</sub>Mn<sub>1-x</sub>O<sub>2-y</sub> Wet Oxidation Catalysts. *Appl. Surf. Sci.* **2002**, *195*, 236–250.
- (37) Liu, X. W.; Zhou, K. B.; Wang, L.; Wang, B. Y.; Li, Y. D. Oxygen Vacancy Clusters Promoting Reducibility and Activity of Ceria Nanorods. *J. Am. Chem. Soc.* **2009**, *131*, 3140–3141.
- (38) Liu, F. D.; He, H. Structure–Activity Relationship of Iron Titanate Catalysts in the Selective Catalytic Reduction of NO<sub>x</sub> with NH<sub>3</sub>. *J. Phys. Chem. C* **2010**, *114*, 16929–16939.
- (39) Liu, F. D.; He, H.; Ding, Y.; Zhang, C. B. Effect of Manganese Substitution on the Structure and Activity of Iron Titanate Catalyst for the Selective Catalytic Reduction of NO with NH<sub>3</sub>. *Appl. Catal., B* **2009**, *93*, 194–204.
- (40) Richter, M.; Trunschke, A.; Bentrup, U.; Brzezinka, K. W.; Schreier, E.; Schneider, M.; Pohl, M. M.; Fricke, R. Selective Catalytic Reduction of Nitric Oxide by Ammonia over Egg-Shell MnO<sub>x</sub>/NaY Composite Catalysts. *J. Catal.* **2002**, *206*, 98–113.
- (41) Zhu, Z. P.; Liu, Z. Y.; Niu, H. X.; Liu, S. J. Promoting Effect of SO<sub>2</sub> on Activated Carbon-Supported Vanadia Catalyst for NO Reduction by NH<sub>3</sub> at Low Temperatures. *J. Catal.* **1999**, *187*, 245–248.
- (42) Shi, A. J.; Wang, X. Q.; Yu, T.; Shen, M. Q. The Effect of Zirconia Additive on the Activity and Structure Stability of V<sub>2</sub>O<sub>5</sub>/WO<sub>3</sub>-TiO<sub>2</sub> Ammonia SCR Catalysts. *Appl. Catal., B* **2011**, *106*, 359–369.
- (43) Wu, Z.; Jiang, B. Q.; Liu, Y.; Zhao, W. R.; Guan, B. H. Experimental Study on a Low-Temperature SCR Catalyst Based on MnO<sub>x</sub>/TiO<sub>2</sub> Prepared by Sol–Gel Method. *J. Hazard. Mater.* **2007**, *145*, 488–494.
- (44) Wu, Z.; Jiang, B. Q.; Liu, Y. Effect of Transition Metals Addition on the Catalyst of Manganese/Titania for Low-Temperature Selective Catalytic Reduction of Nitric Oxide with Ammonia. *Appl. Catal., B* **2008**, *79*, 347–355.
- (45) Marban, G.; Valdes-Solis, T.; Fuertes, A. B. Mechanism of Low-Temperature Selective Catalytic Reduction of NO with NH<sub>3</sub> over Carbon-Supported Mn<sub>3</sub>O<sub>4</sub> Role of Surface NH<sub>3</sub> Species: SCR Mechanism. *J. Catal.* **2004**, *226*, 138–155.
- (46) Kijlstra, W. S.; Brands, D. S.; Smit, H. I.; Poels, E. K.; Blik, A. Mechanism of the Selective Catalytic Reduction of NO with NH<sub>3</sub> over MnO<sub>x</sub>/Al<sub>2</sub>O<sub>3</sub>. *J. Catal.* **1997**, *171*, 219–230.
- (47) Kijlstra, W. S.; Brands, D. S.; Poels, E. K.; Blik, A. Mechanism of the Selective Catalytic Reduction of NO by NH<sub>3</sub> over MnO/Al<sub>2</sub>O<sub>3</sub>. *J. Catal.* **1997**, *171*, 208–218.
- (48) Koebel, M.; Elsener, M.; Madia, G. Reaction Pathways in the Selective Catalytic Reduction Process with NO and NO<sub>2</sub> at Low Temperatures. *Ind. Eng. Chem. Res.* **2001**, *40*, 52–59.
- (49) Zhang, D. S.; Zhang, L.; Fang, C.; Gao, R. H.; Qian, Y. L.; Shi, L. Y.; Zhang, J. P. MnO<sub>x</sub>-CeO<sub>x</sub>/CNTs Pyridine–Thermally Prepared via a Novel in Situ Deposition Strategy for Selective Catalytic Reduction of NO with NH<sub>3</sub>. *RSC Adv.* **2013**, DOI: 10.1039/C3RA41400K.
- (50) Machida, M.; Uto, M.; Kurogi, D.; Kijima, T. MnO<sub>x</sub>-CeO<sub>2</sub> Binary Oxides for Catalytic NO<sub>x</sub> Sorption at Low Temperatures. Sorptive Removal of NO<sub>x</sub>. *Chem. Mater.* **2000**, *12*, 3158–3164.